



Deposition of CdSeTe alloys using CdTe—CdSe mixed powder source material in a close-space sublimation process

Ali Çiriş^{1,2}, Bülent M. Başol³, Yavuz Atasoy^{1,4}, Abdullah Karaca⁵, Tayfur Küçükömeroğlu⁵, Murat Tomakin⁶, and Emin Bacaksız^{5,*}

¹Nanotechnology Application and Research Center, Niğde Ömer Halisdemir University, 51240 Niğde, Turkey

²Department of Renewable Energy Sources/Technologies, Karadeniz Technical University, 61080 Trabzon, Turkey

³Active Layer Parametrics, Scotts Valley, CA 95066, USA

⁴Niğde Ömer Halisdemir University, Niğde Zübeyde Hanım Vocational School of Health Services, Niğde 51240, Turkey

⁵Department of Physics, Karadeniz Technical University, 61080 Trabzon, Turkey

⁶Faculty of Arts and Sciences, Recep Tayyip Erdoğan University, 53100 Rize, Turkey

Received: 30 December 2020

Accepted: 23 February 2021

Published online:

10 March 2021

© The Author(s), under exclusive licence to Springer Science+Business Media, LLC, part of Springer Nature 2021

ABSTRACT

CdSe_xTe_{1-x} films were deposited using a close-space sublimation (CSS) method and CdSe + CdTe mixed powders as the source material. Composition of the source was changed to obtain films with varying x values, and the resulting films were characterized by XRD, SEM, photoluminescence, Raman and optical transmission measurements. All data agreed with the fact that as the Se content of the source material was increased, the composition parameter x also increased. GI-XRD measurements showed the films to be graded in composition, the surface region being more Se-rich. Band gap values obtained from optical measurements showed a minimum band gap of about 1.4 eV for the material that had the highest Se content of about 45% near its top surface. Energy gap vs composition data demonstrated the expected bowing effect in band gap values and a bowing parameter of 0.678 was determined.

1 Introduction

In order to meet the increasing energy demand due to civilization and population growth, the need for renewable and clean energy instead of traditional fossil fuels pay attention in effort to restrain increment of global warming. In this regard, the use of thin film photovoltaic technologies such as CIG(S,Se)

[1], CZT(S,Se) [2] and CdTe [3] has been developed up in the last few decades. In particular, CdTe a group IIB-VIA semiconductor material has been extensively studied for solar cell applications due to its superior properties such as ease of manufacturing, low-cost production and near-optimum band gap (1.5 eV) [3]. The yearly photovoltaic module production of CdTe has exceeded 5 GW, and this

Address correspondence to E-mail: eminb@ktu.edu.tr

manufacturing capacity is expected to expand over 20% by 2024 [4]. Record efficiency of CdTe solar cell has been improved to over 22% by First Solar, with a graded $\text{CdSe}_x\text{Te}_{1-x}$ layer at the window layer of the cell, which enables band gap engineering [5, 6].

Recently, potential benefits of CdSe inclusion into CdTe solar cell structure were pointed out [7] and studies have shown that the band gap of the CdSeTe alloy resulting from reaction of CdTe with Se decreases the band gap near the junction to ~ 1.4 eV. This shift in the band gap of the solar cell stack allows better response of the device at long wavelength region [8]. In the commonly used superstrate configuration, the modified device stack is either formed by depositing a $\text{CdSe}_x\text{Te}_{1-x}$ layer between the buffer layer and the CdTe absorber, or by inserting a CdSe layer that reacts with CdTe forming the $\text{CdSe}_x\text{Te}_{1-x}$ interlayer during the traditional CdCl_2 treatment [9, 10]. In art studies on solar cells using the CdSeTe/CdTe deposition sequence, it was determined that the CdSeTe layer significantly improved cell performance [11, 12]. $\text{CdSe}_x\text{Te}_{1-x}$ thin films have been prepared by various methods such as vacuum evaporation [13, 14], hot wall deposition [15] and co-sputtering [16, 17]. An attractive way of depositing CdTe is close-space sublimation (CSS) which involves compound deposition onto a substrate placed in close proximity to the CdTe source [18]. It should be noted that high efficiency CdTe-based devices have been fabricated using this technique [19, 20].

In this study, we deposited $\text{CdSe}_x\text{Te}_{1-x}$ thin films using well-mixed CdSe and CdTe powders as source material in a CSS system in a single pump-down. We report a study of the effects of Se content on the structural and optical properties of polycrystalline $\text{CdSe}_x\text{Te}_{1-x}$ ($x = 0-1$) thin films. Our results demonstrate an alternative route of depositing $\text{CdSe}_x\text{Te}_{1-x}$ layers to be employed in CdTe-based solar cell applications.

2 Experimental details

Polycrystalline $\text{CdSe}_x\text{Te}_{1-x}$ thin films were deposited on glass substrates by a CSS method. The experimental procedure is shown in Fig. 1. High purity CdSe (99.99%) and CdTe (99.995%) powders were used instead of CdSeTe alloy as the source material in this study. First, the amount of CdSe and CdTe powders in the mix were theoretically calculated to

obtain variable stoichiometry thin films. However, since the sublimation temperatures of CdSe and CdTe [21] are different under the same experimental conditions, it became clear that extra CdSe needed to be used in a fixed amount of CdTe + CdSe powder to target a desired composition. $\text{CdSe}_x\text{Te}_{1-x}$ thin films were grown on soda lime glass at 0.85 mT in Ar atmosphere for 3 min. Source and substrate temperatures were adjusted to 680 °C and 600 °C, respectively. The thickness of the grown films was about 5 μm . Five different alloy films with increasing Se content were produced and these samples were labeled as CdSeTe-1, CdSeTe-2, CdSeTe-3, CdSeTe-4 and CdSeTe-5 in the order of increased Se content. Additionally, non-alloyed CdTe and CdSe thin films were also grown for comparison.

The thickness of the samples was measured with Dektak XT profilometer. XRD spectra were obtained with Rigaku Smartlab diffractometer in the range of $2\theta = 10^\circ-70^\circ$ using CuK_α radiation. Raman spectra and photoluminescence measurements were taken with a Renishaw Confocal Raman microscope at the wavelength of 633 nm at room temperature. The surface morphology of the samples was obtained by Zeiss EVO LS10 SEM. Optical measurements were taken Dongwoo Optron UV-Vis spectrophotometer.

3 Result and discussions

3.1 XRD spectra

Figure 2 shows the XRD spectra of the $\text{CdSe}_x\text{Te}_{1-x}$ films between 20° and 65° . As can be seen from this figure, CdTe and CdSeTe samples have cubic crystalline structure and (111) preferred orientation, as indexed by the (111), (220), (311), (400) and (331) peaks [JCPDS Card No: 00-015-0770]. However, it can also be observed that the CdSe film crystallized in a hexagonal wurtzite structure with a preferred orientation along (002) [JCPDS Card No:00-008-0459]. This is determined by the peak at $2\theta = 45.8^\circ$, which corresponds to the (103) plane of CdSe. In some previous studies, evaporated CdSe films were found to have the cubic structure [22, 23]. In the present study, films were in the more stable hexagonal phase since the substrate temperature was over 550 °C.

Figure 3 shows an expanded view of the XRD peaks in the $2\theta = 23-26^\circ$ range. As can be seen, as the Se-concentration increases, the peak positions are

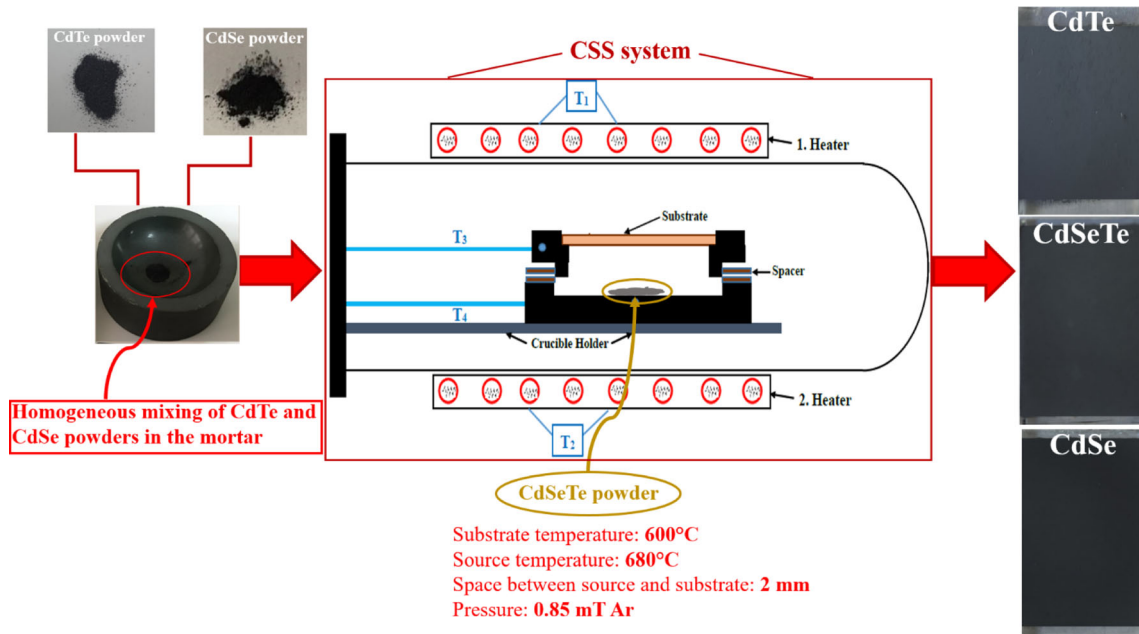


Fig. 1 Schematic representation of experimental procedure

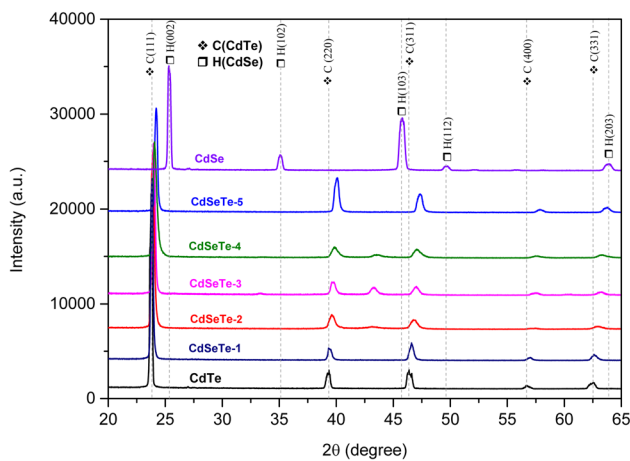


Fig. 2 XRD spectra of all samples measured between 20° and 65°

shifting to higher angles and the intensity of the main peaks decreases. It was observed that all CdSeTe samples crystallized in the cubic phase unlike the CdSe layer. Our findings are in agreement with prior studies that observed hexagonal CdSeTe film formation for Se amount exceeding 40% [3, 15]. If we assume uniform composition for the films the peak position of the CdSeTe-5 film suggests a Se content of about 30% ($x = 0.3$). The clear shift in the XRD peaks is proof that the overall stoichiometry could be controlled in our mixed source CSS approach. To check if there is Se gradient in the films, glancing angle XRD (GI-XRD) measurements were taken and such

gradient was confirmed. The results for sample CdSeTe-5 are shown in Fig. 4, as an example. As can be seen from this data the (111) peak position shifts from 24.50° to 24.25° as the glancing angle is changed from 0.7° to 7°. This corresponds to a compositional range of 30–45% Se and indicates the presence of a compositional gradient in the films.

By using Bragg’s law and the crystal structure equations, lattice parameters of the CdTe- CdSeTe and CdSe can be calculated using Eq. (1a) and Eq. (1b), respectively.

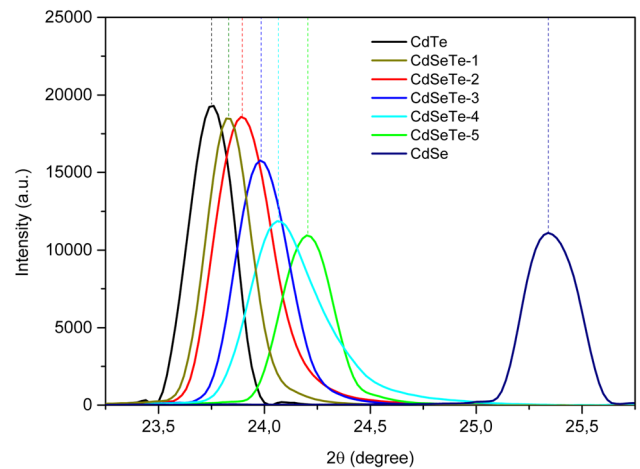


Fig. 3 XRD graphic showing expanded peak positions of samples

$$\frac{1}{d^2} = \frac{h^2 + k^2 + l^2}{a^2} \quad \text{for cubic structure} \quad (1a)$$

$$\frac{1}{d^2} = \frac{4}{3} \frac{(h^2 + hk + k^2)}{a^2} + \frac{l^2}{c^2} \quad \text{for hexagonal structure} \quad (1b)$$

where h , k , l are Miller indices, d is the inter-planar distance and a and c are the lattice parameters. Lattice parameters calculated from the data are shown in Table 1. Experimental and theoretical lattice constants are comparable. The lattice parameter decreases from 6.481 Å for the CdTe sample to 6.362 Å for CdSeTe-5 sample. These values are in agreement with the previous studies [3, 13].

The average crystal size of the samples was calculated from the Scherrer formula [24] given by Eq. (2);

$$D = \frac{K\lambda}{\beta_{hkl} \cos \theta} \quad (2)$$

where K is the Scherrer constant ($K = 0.86$), λ is the X-ray wavelength ($\lambda = 1.5406$ Å), β_{hkl} is the full width at half maximum (FWHM) and θ is the Bragg's diffraction angle. K -constant varies depending on the crystallite shape and size distribution, indices of the diffraction line and is in the range of 0.62 and 2.08. In this study, $K = 0.86$ for cubic crystallites in preferential direction (111) was used. However, since the exact value of Scherrer's constant is not known, the calculated crystal size values are estimated values [25]. Micro-strain values were also calculated using Eq. (3) [26]

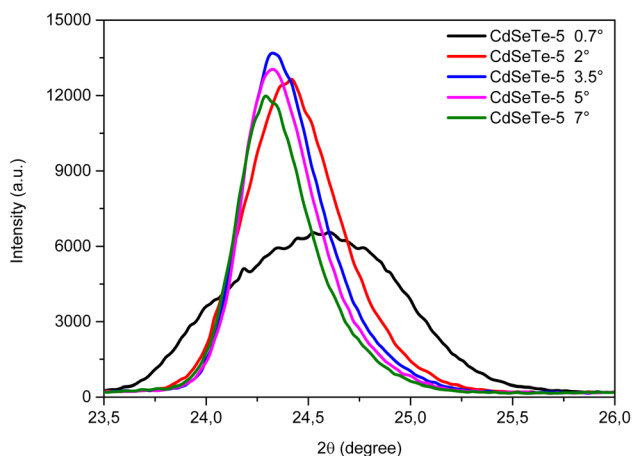


Fig. 4 Expanded XRD spectra of CdSeTe-5 sample at different incident angles (in the range of 0.7–7°)

Table 1 Lattice parameters of the samples

Sample	a (Å)
CdTe	6.483 (C)
CdSeTe-1	6.461 (C)
CdSeTe-2	6.445 (C)
CdSeTe-3	6.421 (C)
CdSeTe-4	6.399 (C)
CdSeTe-5	6.362 (C)
CdSe	4.299 (H) 7.010 (H)

$$\varepsilon = \frac{\beta_{hkl} \cos \theta}{4} \quad (3)$$

where ε is the root mean square value of micro-strain. The crystallite size and micro-strain values calculated using Eqs. (2–3) are shown in Table 2. As can be seen from this data, the largest crystallite value is 32 nm (for CdTe). However, as the Se-concentration increases, crystallite size decreases down to 24 nm. On the contrary, it was determined that micro-strain values increase from the low value of 0.00101 (for CdTe) to 0.00132 (for CdSeTe-5) as Se content increases. This inverse relationship between the crystallite size and micro-strain can be clearly seen in Fig. 5.

3.2 Raman spectra

Figure 6 shows the Raman spectra obtained from all samples, measured at room temperature, excited by 633 nm HeNe laser. As can be seen in this figure, CdTe-like and CdSe-like transverse optical (TO) and longitudinal optical (LO) phonons have been detected in the data between 100 cm^{-1} and 220 cm^{-1} . In addition, frequencies of the second-order LO phonons are also observed between 300 cm^{-1} and 425 cm^{-1} . The peaks centered at 139.8 cm^{-1} and 164.3 cm^{-1} correspond to the fundamental transverse

Table 2 Crystallite size and micro-strain values calculated by using Eq. (2–3)

	D (Crystallite size) (nm)	ε (Micro-strain)
CdTe	32	0.00101
CdSeTe-1	30	0.00107
CdSeTe-2	28	0.00116
CdSeTe-3	27	0.00121
CdSeTe-4	25	0.00126
CdSeTe-5	24	0.00132

optical (TO_1) and longitudinal optical (LO_1) phonon modes of CdTe, and the peak centered at 328.7 cm^{-1} is associated with the longitudinal optical ($2LO_1$) phonon mode of CdTe [27, 28]. When the spectrum of the CdSeTe-1 sample was examined, it was seen that the intensity of the vibrational mode at 164.3 cm^{-1} (CdTe-like LO mode) decreased and its position shifted to a higher frequency (close to 180 cm^{-1}), and a low-intensity shoulder peak associated with CdSe-like LO mode started to show up. As for the behavior of the spectra obtained from CdSeTe-2 through CdSeTe-5 samples, it is seen that the peak at 164.3 cm^{-1} belonging to CdTe disappears and a distinct vibration mode occurs at around 188.8 cm^{-1} . In the Raman spectrum of cubic structures, only LO phonons are permitted. Therefore, TO mode which appears around 139 cm^{-1} for CdSeTe can be attributed to disorder and defects of the alloys [29]. The phonon frequency may also vary depending on the stoichiometry of the alloy, because the lattice parameter of CdSeTe shifts to a value different from the bulk parameters of CdSe and CdTe [30, 31]. As a result, it can be concluded from the data of Fig. 5 that going from CdSeTe-1 sample to CdSeTe-5 sample the overall Se content of the alloy gradually increases, as supported by the XRD data. In the spectrum of CdSe, the two peaks located at 206.7 cm^{-1} and 414.4 cm^{-1} are associated with the longitudinal optical phonon mode (LO mode) [32].

3.3 SEM images

Figure 7 shows the scanning electron microscope (SEM) images of CdTe, CdSeTe-5 and CdSe samples.

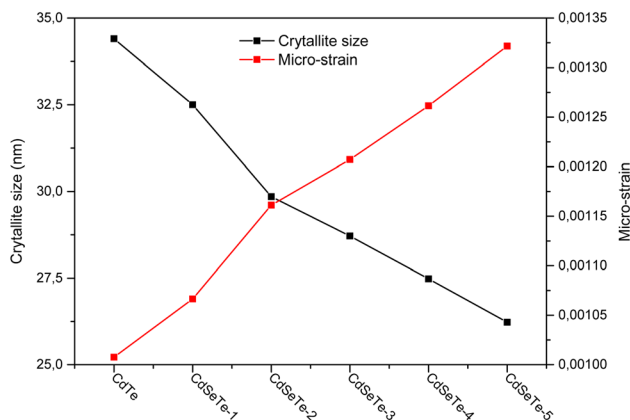


Fig. 5 Crystallite size and micro-strain graphics for CdTe and CdSeTe samples

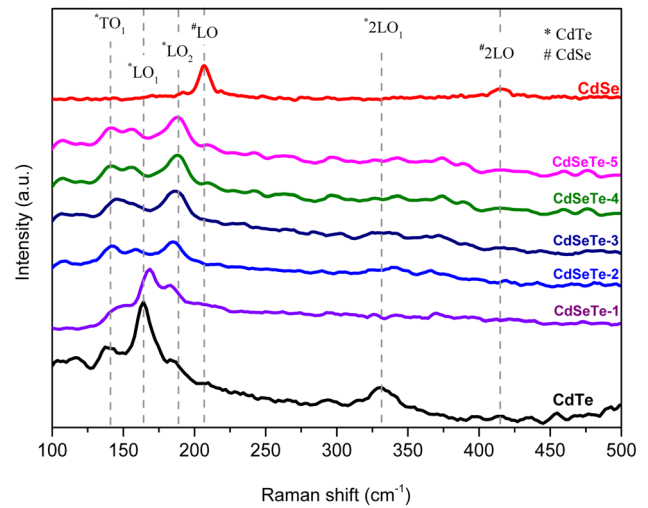


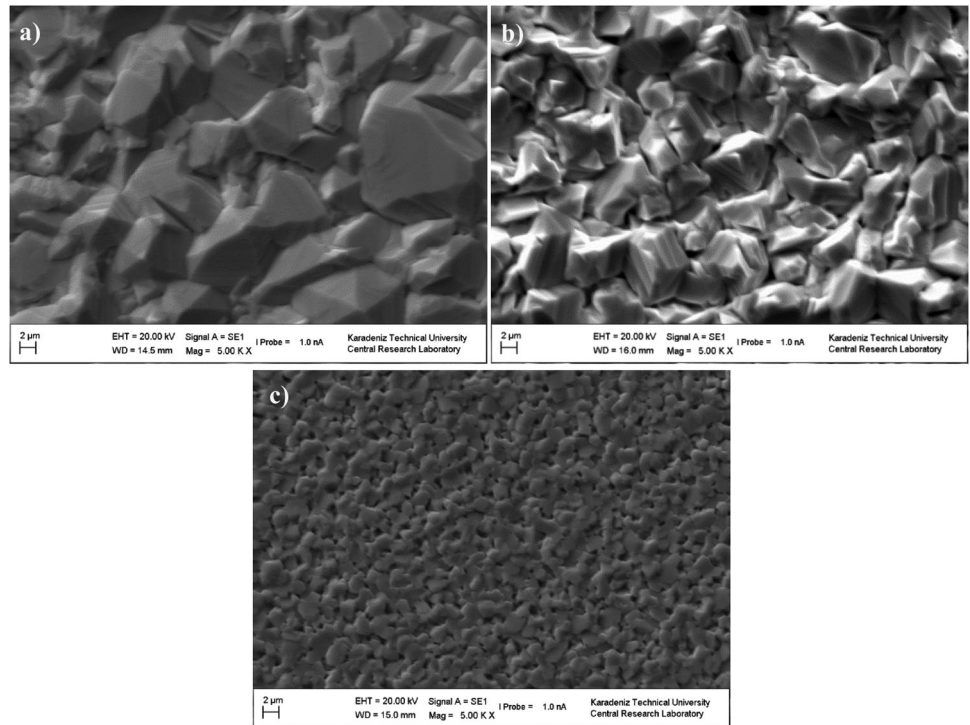
Fig. 6 Raman spectra of all samples measured between 100 cm^{-1} and 500 cm^{-1}

As can be seen from this data, the surface morphology and average particle size of the films strongly vary with the composition. CdTe has a facet-shape grain structure which is densely-packed, homogeneous and free from voids, cracks or pinholes. The size of the grains varies between $3\text{ }\mu\text{m}$ and $14\text{ }\mu\text{m}$. There is no significant change in the grain configuration and compact nature for sample CdSeTe-5. However, the grain size is decreased, varying between about $2\text{ }\mu\text{m}$ and $8\text{ }\mu\text{m}$. CdSe film morphology, on the other hand, is very different than the Te containing compositions. This film has much smaller grain or particle size which is in the range of $1\text{--}3\text{ }\mu\text{m}$. Although relatively small, this grain size is still considerably larger than those observed in CdSe films produced by other methods [33–37]. This is due to the fusion of grains during high temperature deposition by the CSS method [38].

3.4 Photoluminescence spectra

Room temperature photoluminescence (RTPL) data obtained from the CdSe, CdTe and CdSeTe alloy films are shown in Fig. 8. As can be seen, the PL spectrum of the CdSe sample showed a main peak at approximately 718 nm , corresponding to an energy value of 1.73 eV . This peak is attributed to band-to-band transitions in the compound. In the PL spectrum of CdTe, a main peak appears at around 821 nm corresponding to the absorption edge of CdTe (1.51 eV). In the PL spectrum of the CdSeTe samples (from CdSeTe-1 to CdSeTe-5), the peak position shifts

Fig. 7 SEM images of **a** CdTe, **b** CdSeTe-5 and **c** CdSe samples



to higher and higher wavelengths (843 nm, 853 nm, 870 nm, 876 nm and 882 nm) as the Se content increases. These wavelength values correspond to band gap values of 1.471 eV, 1.454 eV, 1.452 eV, 1.416 eV and 1.406 eV, respectively. The results show that as the Se-concentration in the CdSeTe alloy increases, its band gap value decreases due to the bowing effect as reported by others.

3.5 Optical measurements

In order to examine the optical properties of the samples, transmittance measurements were taken in the wavelength range of 500–1000 nm. Band gaps of the samples were calculated employing Eq. (4) and using the transmittance data [39].

$$(\alpha hv) = A(hv - E_g)^{1/2} \tag{4}$$

where ' E_g ' is the optical band gap, ' A ' is proportionality constant, ' hv ' is the photon energy and ' α ' is the absorption coefficient. The absorption coefficients in this equation can be calculated by means of Eq. (5).

$$\alpha = \frac{1}{d} \ln\left(\frac{1}{T}\right) \tag{5}$$

where ' d ' is the thickness in cm and ' T ' is the transmittance. In Fig. 9, the $(\alpha hv)^2 - (hv)$ graphs of all

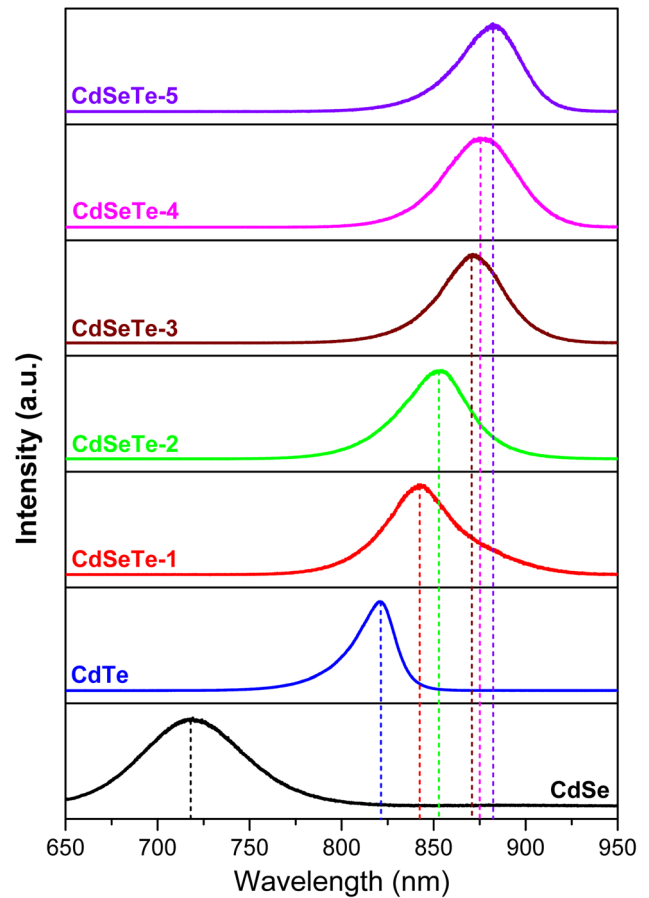


Fig. 8 PL spectra of samples

samples are shown. The band gap values were determined from the x-axis intersection points of the linear parts of the absorption curves. These are listed in Table 3. As can be seen from this table, the band gaps of CdTe (1.473 eV) and CdSe (1.672 eV) are in agreement with known properties of these compounds. As for the CdSeTe samples, it is seen that the band gap value decreases as the Se-concentration in the alloy increases in agreement with the photoluminescence results. In the CdSeTe-5 sample, a minimum band gap value (1.397 eV) was reached. This value is similar to the value obtained from photoluminescence measurement.

It should be noted that the optical measurements reported above are expected to be sensitive to and dominated by the lowest energy gap in a graded film. XRD measurements taken at high incident angles, however, are expected to be dominated by the composition that represents the largest amount within the film. We had previously pointed out that glancing angle XRD of sample CdTeSe-5, for example, indicated a maximum Se concentration of about 45% near the surface when the incident angle was 0.7°, whereas at 7° the peak position suggested a Se content of 30%. The band gap value obtained from optical measurements for this sample is about 1.4 eV, which is more in line with a Se composition of 45%. Therefore, we used the near surface composition obtained from glancing angle measurements made on all samples for the E_g - x graph plotted in the inset of Fig. 9. When the polynomial fit is matched, it is clearly seen from this plot that the band gap is minimum at around $x = 0.45$ and the band gap increases for x values larger than 0.45, due to the bowing effect. Second-

Table 3 Band gaps of CdSe_xTe_{1-x} thin films

Sample	Band gap (eV)
CdTe	1.473
CdSeTe-1	1.448
CdSeTe-2	1.425
CdSeTe-3	1.404
CdSeTe-4	1.399
CdSeTe-5	1.397
CdSe	1.672

order polynomial function describing the dependence of the band gap on the composition is usually written as

$$E_G(x) = E_G^{CdTe}(1 - x) + E_G^{CdSe}x - bx(1 - x) \tag{6}$$

where E_G is band gap, x is Se% composition with respect to (Se + Te) and b is the bowing parameter. According to our findings, the polynomial fit function can be written as:

$$E_G(x) = 1.481 - 0.457x + 0.647x^2 \tag{7}$$

By rearranging the above equation;

$$E_G(x) = 1.481(1 - x) + 1.671x - 0.647x(1 - x) \tag{8}$$

In this Equation 1.481 and 1.671 are the band gap values of CdTe and CdSe, respectively, and 0.647 is the bowing parameter. The calculated band gaps and bowing parameter using the equation of polynomial curve (Eq. 8) are in agreement with prior art reported for films grown by other techniques [40, 41].

Several studies in the literature support the band gap bending behavior in CdSeTe alloys [8, 41, 42]. In one of the studies investigating the electronic band structures of the CdSe_xTe_{1-x} alloy, it was determined that the degree of ionicity of all atoms changes linearly with the x -ratio. They revealed that there was strong competition between anions (Se and Te) in trapping/loss charges and this competition was the basic cause of the bowing effect [42].

4 Conclusions

CdTe, CdSe_xTe_{1-x} and CdSe films were grown by CSS method by using a mixed CdSe + CdTe powder source. Mixing ratios were changed to obtain films with varying compositions. XRD spectra indicated that CdTe and CdSeTe films with < 50% Se crystallized in cubic structure and the CdSe film had hexagonal structure. Furthermore, Se inclusion into

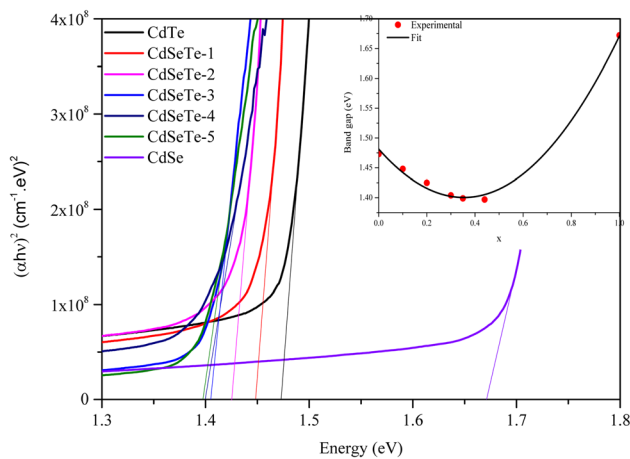


Fig. 9 $(\alpha hv)^2 - (hv)$ graph of all of the samples

the CdTe lattice was apparent from XRD peak position shifts as the Se amount in the source material was increased. Raman spectra data also agreed with this finding. GI-XRD data showed that there was compositional gradient in these films yielding higher Se content near the top surface. SEM images showed that samples produced by the CSS method were large-grained and compact. Grain size reduced as the Se amount was increased from 0 to 100%. Photoluminescence spectra indicated peaks associated with band to band transitions, which could be translated into band gap values that got smaller as Se content increased. Tauc plots were generated using optical transmittance data. Band gap values obtained agreed with the photoluminescence results, and they represented the lowest band gap material present in these graded films. E_g - x relationship demonstrated band gap bowing effect that yielded the smallest band gap value of ~ 1.4 eV for the film that comprised $x = 0.45$ composition.

Acknowledgements

This work is financially supported by the Scientific and Technological Research Council of Turkey (TUBITAK) with the grant number of 118F140.

References

- P. Jackson, D. Hariskos, E. Lotter et al., Prog. Photovoltaics Res. Appl. **19**, 894 (2011)
- S.S. Patil, R.M. Mane, S.S. Mali, C.K. Hong, P.N. Bhosale, Sol. Energy **201**, 102 (2020)
- D.E. Swanson, J.R. Sites, W.S. Sampath, Sol. Energy Mater. Sol. Cells **159**, 389 (2017)
- ASB Ankit Gupta (2017) Global Market Insights,
- A.H. Munshi, J. Kephart, A. Abbas et al., IEEE Journal of Photovoltaics **8**, 310 (2017)
- M.A. Green, E.D. Dunlop, D.H. Levi, J. Hohl-Ebinger, M. Yoshita, A.W. Ho-Baillie, Prog. Photovoltaics Res. Appl. **27**, 565 (2019)
- B.M. Başol, B. McCandless, Journal of Photonics for Energy **4**, 040996 (2014)
- M. Lingg, S. Buecheler, A.N. Tiwari, Coatings **9**, 520 (2019)
- J.D. Poplawsky, W. Guo, N. Paudel et al., Nat. Commun. **7**, 1 (2016)
- T. Wang, X. Zhu, W. Li, J. Zhang, W. Wang, J. Alloy. Compd. **828**, 154415 (2020)
- T. Ablekim, J.N. Duenow, X. Zheng et al., ACS Energy Letters **5**, 892 (2020)
- T. Ablekimy, J. Duenow, H. Moutinho, et al. (2020) 2020 47th IEEE Photovoltaic Specialists Conference (PVSC)IEEE,
- M. Lingg, A. Spescha, S.G. Haass, R. Carron, S. Buecheler, A.N. Tiwari, Sci. Technol. Adv. Mater. **19**, 683 (2018)
- T. Santhosh, K.V. Bangera, G. Shivakumar, Sol. Energy **153**, 343 (2017)
- N. Muthukumarasamy, S. Jayakumar, M. Kannan, R. Balasundaraprabhu, Sol. Energy **83**, 522 (2009)
- C. Li, A. Wang, L. Wu et al., Materials Research Express **6**, 066415 (2019)
- N. Shrestha, C.R. Grice, E. Bastola et al., MRS Advances **3**, 3293 (2018)
- A.N. Tiwari, G. Khrypunov, F. Kurdzesau, D. Bätzner, A. Romeo, H. Zogg, Prog. Photovoltaics Res. Appl. **12**, 33 (2004)
- J. Britt, C. Ferekides, Appl. Phys. Lett. **62**, 2851 (1993)
- T. Aramoto, S. Kumazawa, H. Higuchi et al., Jpn. J. Appl. Phys. **36**, 6304 (1997)
- Y.-R. Luo, *Comprehensive Handbook of Chemical Bond Energies* (CRC Press, 2007).
- S.S. Priya, B.L. Shree, P.T. Ranjani, P. Karthick, K. Jeyadheepan, M. Sridharan, Materials Today: Proceedings **3**, 1487 (2016)
- A. Purohit, S. Chander, S. Nehra, M. Dhaka, Physica E **69**, 342 (2015)
- P. Scherrer, Nachrichten von Der Gesellschaft Der Wissenschaften Zu Göttingen Math. Klasse. **26**, 98 (1918)
- J.I. Langford, A. Wilson, J. Appl. Crystallogr. **11**, 102 (1978)
- S. Lalitha, R. Sathyamoorthy, S. Senthilarasu, A. Subbarayan, K. Natarajan, Sol. Energy Mater. Sol. Cells **82**, 187 (2004)
- Z. Feng, P. Becla, L. Kim et al., J. Cryst. Growth **138**, 239 (1994)
- N.K. Das, S. Farhad, J. Chakaraborty et al., International Journal of Renewable Energy Research (IJRER) **10**, 293 (2020)
- D.N. Talwar, Z.C. Feng, J.-F. Lee, P. Becla, Physical Review B **87**, 165208 (2013)
- Z. Chai, W. Wu, D. Kong, Y. Gao, Q. Chang, J. Non-Cryst. Solids **382**, 121 (2013)
- L.X. Hung, P.D. Bassène, P.N. Thang et al., RSC advances **7**, 47966 (2017)
- C. Bijumon, V.S. Kumar, Int. J. Sci. Technol. Res **4**, 1 (2015)
- K. Sarmah, R. Sarma, H. Das, Chalcogenide Letters **5**, 153 (2008)
- N. Gopakumar, P. Anjana, P.V. Pillai, J. Mater. Sci. **45**, 6653 (2010)
- A. Çiriş, B. Başol, S. Yılmaz et al., Mater. Sci. Semicond. Process. **91**, 90 (2019)

36. A. Yadav, M. Barote, E. Masumdar, *Mater. Chem. Phys.* **121**, 53 (2010)
37. S. Vishwakarma, A. Kumar, S. Prasad, R. Tripathi (2013) *Chalcogenide Letters* 10.
38. C.V. Thompson, *Annu. Rev. Mater. Sci.* **20**, 245 (1990)
39. J. Tauc, R. Grigorovici, A. Vancu, *Physica Status Solidi* **15**, 627 (1966)
40. R. Islam, H. Banerjee, D. Rao, *Thin Solid Films* **266**, 215 (1995)
41. S.-H. Wei, S. Zhang, A. Zunger, *J. Appl. Phys.* **87**, 1304 (2000)
42. N. Tit, I.M. Obaidat, H. Alawadhi, *J. Phys.: Condens. Matter* **21**, 075802 (2009)

Publisher's Note Springer Nature remains neutral with regard to jurisdictional claims in published maps and institutional affiliations.